Journal of Materials Chemistry A

ROYAL SOCIETY OF CHEMISTRY

PAPER

View Article Online
View Journal | View Issue

Cite this: J. Mater. Chem. A, 2024, 12, 21310

Enhanced photoelectrochemical nitrogen reduction to ammonia by a plasmon-active Au grating decorated with the gC_3N_4@MoS_2 heterosystem and plasmon-active nanoparticles†

Denis Zabelin, *[a] Anastasiia Tulupova,[a] Anna Zabelina,[a] Andrea Tosovska,[a] Rashid Valiev,[b] Ruslan Ramazanov,[b] David Mares,[c] Vitezslav Jerabek,[c] Vasilii Burtsev,[a] Mariia Erzina,[a] Alena Michalcová,[d] Anastasiia Skvortsova,[a] Vaclav Svorcik[a] and Oleksiy Lyutakov[a]

The electrochemical production of ammonia from nitrogen (so-called nitrogen reduction reaction – NRR) is one of the key tasks of modern electrochemistry. The use of photo-electrochemical approaches in the NRR allows the involvement of renewable sunlight energy and partially reduces the energy demand of the NRR process and increases its efficiency. For efficient photoelectrochemical NRR realization, a rational design of the photoelectrode used is required. In this work, we propose the design, creation, and optimization of a hybrid electrode, based on utilization of coupled 2D semiconductors and plasmonic hot spots. In our approach, the gC_3N_4@MoS_2 semiconductor (in the form of 2D flakes), with high catalytic activity towards the NRR is used as a redox-active material. For the involvement of sunlight energy, plasmon triggering is used in two modes: simple plasmonic triggering using a periodic Au grating and coupled plasmon triggering through the sandwiching of 2D gC_3N_4@MoS_2 flakes between the Au grating and different plasmon active nanoparticles (gold and silver nanoparticles with different shapes). We also carried out a series of calculations (including finite difference time domain estimation of plasmon energy distribution and density functional calculation) aimed at the estimation of the local value of plasmon energy and the NRR process under conditions of plasmon triggering. As a result of careful design and photoelectrode optimization, we were able to achieve 882.1 μg h^{-1} mg_{cat}^{-1} ammonia yield and 22.1% faradaic efficiency. The proposed photoelectrode design makes it possible to effectively use both the catalytic properties of the coupled semiconductors and the strengths of plasmon-assisted triggering.

Received 14th May 2024
Accepted 10th July 2024

DOI: 10.1039/d4ta03350g

rsc.li/materials-a

Introduction

Ammonia (NH_3) is an essential component in the production of numerous ammonium fertilizers. Recently, it was also proposed as an eco-friendly hydrogen carrier in the form of chemical bonds.[1–6] Today, the fundamental reaction for ammonia production is the Haber–Bosch process, which however is unfavoured by high energy demands, hard synthesis conditions and utilization of fossil hydrogen.[7–10] Such synthesis conditions can be related to the high nitrogen binding energy (941 kJ mol^{-1}), non-polarity of the molecule and low polarization ability.[7,11,12] In order to substitute the Haber–Bosch process and find a more acceptable alternative for ammonia production[13] the electrochemical nitrogen reduction to ammonia is actually studied. The nitrogen reduction reaction (NRR) can be performed at atmospheric pressure with utilization of potentially renewable energy sources. Moreover, the NRR utilizes water as a source of hydrogen atoms, eliminating in this way the necessity of using fossil hydrogen.[14–17] To date, the electrochemical NRR to ammonia is the most promising alternative for real-life applications because of its relatively high efficiency and flexibility.[18,19]

A large number of catalysts for the NRR process have been reported.[20–27] However, almost all of them show low catalytic activity, reflected in low NH_3 yield and low faradaic efficiency (FE) values. There are several approaches to increase the efficiency of nitrogen reduction electrochemically, such as defect

[a]Department of Solid State Engineering, University of Chemistry and Technology, 16628 Prague, Czech Republic. E-mail: denis.zabelin@vscht.cz
[b]Department of Chemistry, University of Helsinki, FI-00014 Helsinki, Finland
[c]Department of Microelectronics, Czech Technical University, Prague, 16600, Czech Republic
[d]Department of Metals and Corrosion Engineering, University of Chemistry and Technology, 16628 Prague, Czech Republic

† Electronic supplementary information (ESI) available. See DOI: https://doi.org/10.1039/d4ta03350g.

engineering,[28,29] heteroatom doping,[30–32] concurrent hydrogen evolution reaction suppression, *etc.*[20–35] However, the effectiveness of current materials and approaches is still far from optimal, and they cannot be applied for ammonia production from nitrogen on an industrial scale.[36,37]

Utilization of cheap and renewable (sun)light is another approach to increase the efficiency of nitrogen-to-ammonia conversion.[38–42] A few materials and structures have recently been used for the photoelectrochemical NRR.[43–45] Because of the redox activity of photo-excited charge carriers, most of these materials utilize the UV part of the sunlight spectrum but the utilization of near-infrared (NIR) wavelength from the solar spectrum is of greatest interest for photo-electrochemical processes, including the NRR.[46–52] Plasmon-based photosensitization is one of the promising ways to utilization of almost all wavelengths from the sunlight spectrum in the NRR.[53–56]

So, actually intensive current research is being focused on NRR efficiency enhancement by utilization of plasmon triggering.[57–62] In turn, the plasmon effect on the photoelectrocatalytic reaction efficiency can be greatly enhanced by careful design of plasmon-active nanostructures (in particular – by creation of coupled plasmon nanostructures), which allows a gigantic value of local, plasmon-related, electric field (EF) to be achieved.[63–68] Nevertheless, until now, plasmon coupling has mostly been applied in photoelectrochemical water splitting or CO_2 reduction[69,70] but not in the NRR.

Recently, our research group demonstrated that LSP–SPP coupling under sunlight illumination significantly increases the nitrogen to ammonia conversion rate and faradaic efficiency.[71] In this work, we describe an alternative design of NRR photoelectrodes, with enhanced redox-active coupled 2D materials and effective plasmon coupling, based on the experimental and theoretical choice of suitable plasmon active nanoparticles.

Experimental

A detailed description of used materials, sample preparation and characterization is given in the ESI.† Briefly, gC_3N_4 flakes were synthesized by urea annealing in air with subsequent delamination and purification. MoS_2 was prepared by hydrothermal approaches from corresponding precursors (sodium molybdate dihydrate and thiourea) in the presence of gC_3N_4 flakes. To obtain 2D nanosheets of gC_3N_4@MoS_2, the resulting powder was subjected to liquid nitrogen exfoliation followed by ultrasound treatment. The gold grating, responsible for the excitation of surface plasmon polaritons (SPPs), was prepared by sputtering of a 25 nm thick Au layer on a periodic polymer template.[54,71] In the next step, the 2D/2D gC_3N_4@MoS_2 heterostructure was deposited on the Au grating surface using electrophoresis. In the final step, different plasmon active nanoparticles (spherical Au NPs, spherical Ag NPs, cubic Au NPs, urchin-like Au NPs, and triangle Ag NPs) were prepared *via* a wet chemical route and further deposition of gC_3N_4@MoS_2 onto the Au grating surface.

The electrochemical or photo-electrochemical catalytic activities of the samples were studied at room temperature under illumination with a sunlight simulator or in the dark, both using a PalmSens 4 potentiostat (Palm Instruments, Netherlands) in a three-electrode mode and an H-type cell separated by a Nafion membrane. Photoelectrocatalytic N_2 reduction experiments were carried out in chronoamperometric mode in 0.1 M Na_2SO_4 mixture solution which contained 20 wt% ([C_4mpyr][eFAP]) and which was purged with high-purity N_2 gases (purging with Ar or Air was used in control experiments) for 30 min before the experiment and then continuously purged with nitrogen during experiments. The amount of ammonia produced was determined photometrically and calculated using a calibration curve prepared by measuring the adsorption spectra of model solutions using the KIT test.

Results and discussion

Schematic representation of the proposed experimental concept

The scheme of sample preparation is shown in Fig. 1. In the first step, the 2D/2D gC_3N_4@MoS_2 heterostructure was prepared and deposited on the surface of the plasmon-active gold grating (responsible for the SPP excitation). Such structure was utilized for the NRR under "simple" plasmon triggering of gC_3N_4@MoS_2 redox activity. Alternatively, plasmon-active nanoparticles with different shapes and compositions were deposited on the sample surface (*i.e.*, on the surface of Au grating/gC_3N_4@MoS_2 flakes). Plasmon active nanoparticles ensure the excitation of localized surface plasmon resonance (LSP). The 2D nature of catalytically active gC_3N_4@MoS_2 provides appropriate gaps between the Au grating and metal nanoparticles. In the space between plasmon active nanostructures, where the redox active material, gC_3N_4@MoS_2 flakes, is located the plasmon coupling (*i.e.* in SPP–LSP coupling) and energy concentration arise. The utilization of different metal nanoparticles will ensure different efficiencies of plasmon coupling, and in turn different kinetics and efficiencies of the NRR, as was initially assumed.

Characterization of gC_3N_4@MoS_2 flakes

Characterization of gC_3N_4@MoS_2 is presented in Fig. 2. First, FTIR spectra (Fig. 2A) indicate the presence of peaks characteristic of the structure of graphitized carbonitride: 1100–1700 cm^{-1}, responsible for the –C–N– and –C=N– vibrations; 808 cm^{-1} characteristic of triazine rings; and 3100–3300 cm^{-1} responsible for the NH_2-group stretching vibration. The characteristic peaks of MoS_2 (Fig. S1A†) are not well visible due to overlapping with the gC_3N_4 peaks. However, the presence of MoS_2 in the gC_3N_4@MoS_2 heterostructure is well visible from Raman spectra (Fig. 2B) where the peaks characteristic of the MoS_2 E_{2g} and A_{1g} vibration modes (377 and 403 cm^{-1}) appear. Compared with the Raman spectrum of the pristine MoS_2 (Fig. S1B†), the peaks are shifted only slightly, which observation suggests the similar crystal structure of MoS_2 in the gC_3N_4@MoS_2 and control powder. The survey XPS spectrum of gC_3N_4@MoS_2 (Fig. 2C) indicates the presence of both molybdenum and sulphur, as well as carbon and nitrogen from gC_3N_4. Calculated from the survey XPS spectra, the surface elemental composition of gC_3N_4@MoS_2 (as well as control gC_3N_4 and

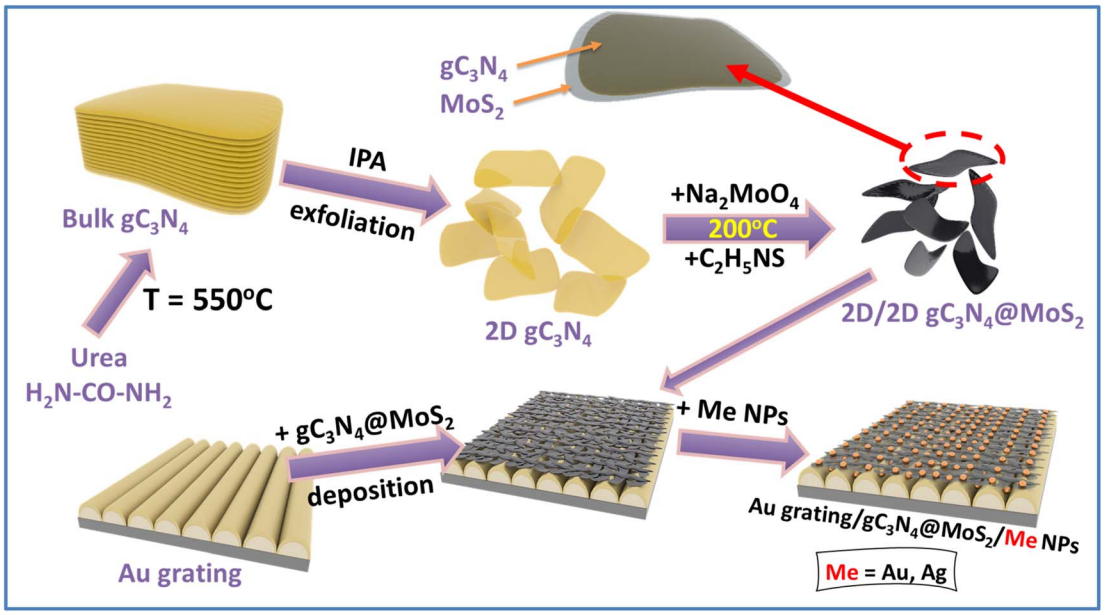

Fig. 1 Schematic representation of sample preparation.

MoS_2) is presented in Table 1. As is evident, the ratio of Mo and S in gC_3N_4@MoS_2 and MoS_2 is close to the stoichiometric one, confirming the correct composition of molybdenum disulfide produced on the gC_3N_4 nanoflake surface. Shifts of Mo $3d_{5/2}$ and $3d_{3/2}$ peaks (in comparison with the control MoS_2 powder) are evident from the high resolution XPS spectra (Fig. S2†). A similar shift can also be observed when comparing the S $2p_{3/2}$ and S $2p_{1/2}$ peaks of both samples. A positive shift in the position of the C 1s peaks from the gC_3N_4@MoS_2 sample in

Table 1 Elemental concentration calculated from XPS spectra

	Elemental concentration (at%)			
Sample	Mo	S	C	N
MoS_2	31.89	68.11	—	—
gC_3N_4	—	—	45.52	54.48
gC_3N_4@MoS_2	20.35	39.31	19.87	20.47

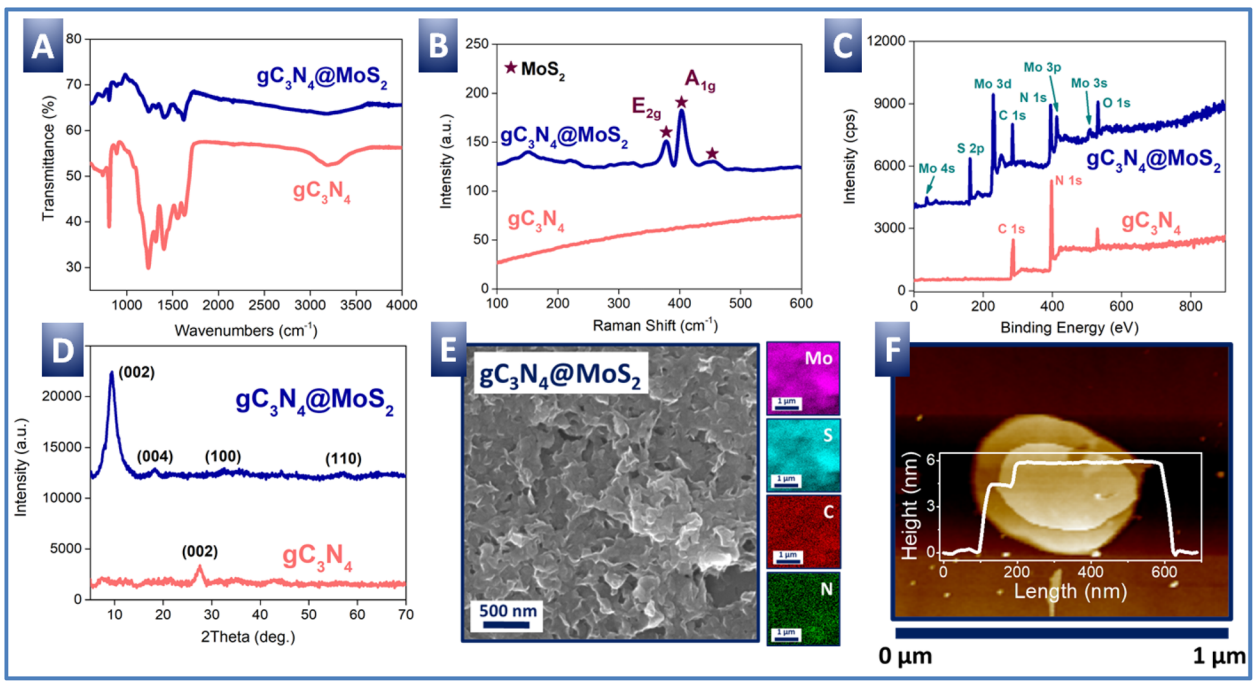

Fig. 2 gC_3N_4@MoS_2 characterization: (A)–(C) FT-IR, Raman, and XPS spectra; (D) XRD patterns; (E) SEM-EDX image with elemental mapping and (F) AFM images of gC_3N_4@MoS_2 flakes and the single flake profile.

comparison with control gC_3N_4 powder is also evident.[72,73] The shifts indicate appropriate semiconductor coupling and related electron transfer from gC_3N_4 to MoS_2.[72,73] Moreover, a slight difference in the E_{2g} and A_{1g} peak positions in the Raman spectra of gC_3N_4@MoS_2 and pure MoS_2 (Fig. 2B and S1B†) also indicates the presence of interfacial electronic interactions (charge transfer) between the gC_3N_4 and MoS_2 phases.[74]

Finally, the XRD pattern (Fig. 2D) confirms the good crystallinity of the gC_3N_4@MoS_2 sample. Peaks at 9.3, 18.2, 32.7, and 56.9° well correspond to the 1T-MoS_2 phase. The main diffraction peak of MoS_2 at 9.3° ((002) plane) in the gC_3N_4@-MoS_2 structure is slightly broader than that from the control MoS_2 sample (Fig. S1D† *vs.* 2D), which broadening indicates a slight decrease of MoS_2 crystallinity, when it was prepared in the presence of amorphous gC_3N_4.

The morphology and 2D structure of the gC_3N_4@MoS_2 structure were checked using SEM-EDX, AFM and HRTEM-EDX methods (Fig. 2E, F and S3†).

The AFM measurements confirm the two-dimensional nature of the gC_3N_4@MoS_2 structure, with two well-coupled flakes with different thicknesses (characteristic structure morphology is presented in Fig. 2F, while Fig. S4† shows the measurements of the samples prepared separately – the measurements were performed at different places). The thickness of the final coupled structure is about 5–6 nm, which is larger compared to that of the control MoS_2 nanoflakes (Fig. S1E†). HRTEM images also confirm the two-dimensional orientation of the samples, whereas the results of Mo, S, C and N EDX mapping show a uniform distribution of these elements in the flake structure (Fig. S3†). Similar results were obtained with the SEM-EDX technique, which indicates that C and N elements (*i.e.* gC_3N_4) are uniformly distributed in the same way as Mo and S, which finding may suggest that the gC_3N_4 structure was indeed a substrate for the growth of the MoS_2 structure in the hydrothermal synthesis (Fig. S5†). So, it can be concluded that the MoS_2 structure is uniformly grown on the gC_3N_4 nanoflake surface.

Characterization of the Au/gC_3N_4@MoS_2 structure

In the next step, the deposition of gC_3N_4@MoS_2 on a plasmon-active Au grating (Fig. S6†) was performed in order to utilize plasmon assistance for the nitrogen reduction reaction (NRR) enhancement. The deposition of gC_3N_4@MoS_2 flakes on the Au grating surface was performed in the electrophoretic regime and resulted in a uniform flake distribution over the entire plasmon-active Au grating area. Evident changes of sample surface morphology after the flake deposition were observed with utilization of AFM and SEM measurements (Fig. 3 and S6†). The grating surface becomes significantly rougher, but its apparent periodicity is conserved, both indicating that the flakes cover grating tops and also penetrate the valleys. Micro-EDX and macro-Raman maps show that the signal from gC_3N_4@MoS_2 is uniformly spread over the sample areas. UV-Vis spectra of created samples are shown in Fig. 3D. The pristine

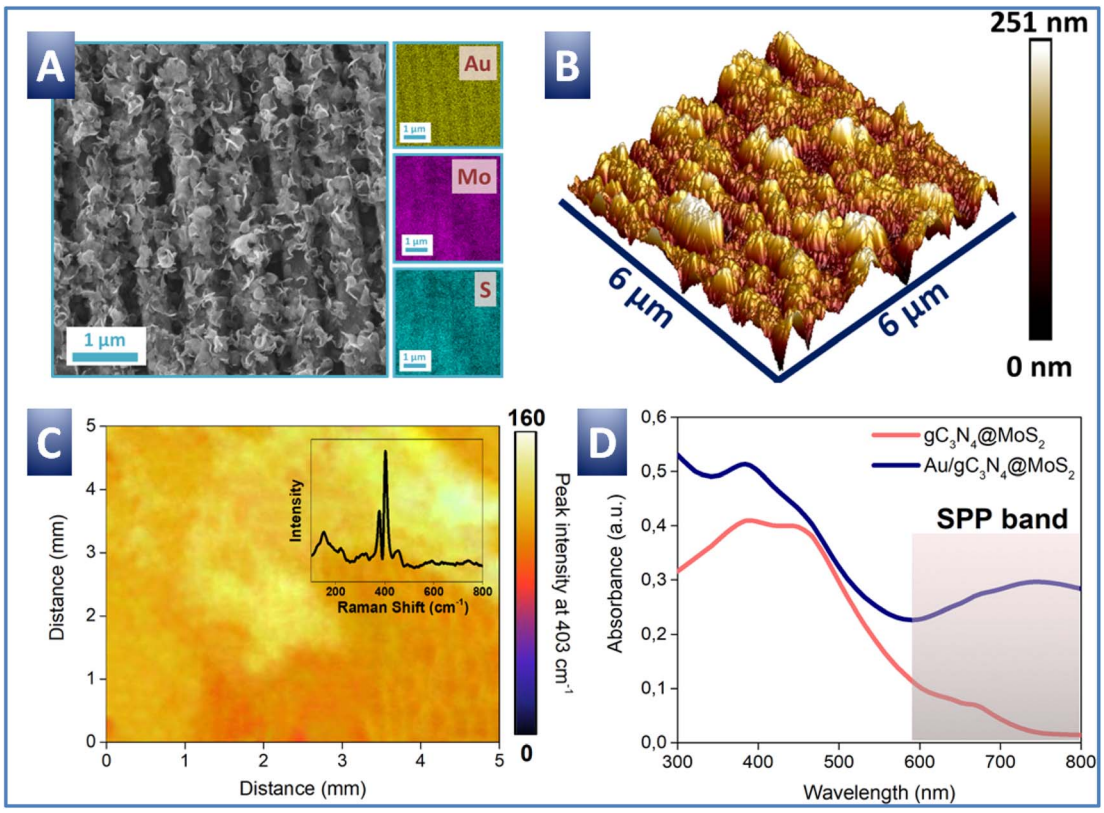

Fig. 3 (A) and (B) SEM-EDX and AFM images of the surface morphology of Au/gC_3N_4@MoS_2; (C) Raman mapping of gC_3N_4@MoS_2 distribution on the Au grating surface; (D) UV-Vis spectra of gC_3N_4@MoS_2 flakes and the Au/gC_3N_4@MoS_2 structure.

gC_3N_4@MoS_2 flakes (measured in suspension) show a wide absorption band, located at shorter wavelengths, and attributed to electron excitation from the valence to the conduction band (photoexcited electrons can subsequently participate in the NRR). Measurements of flakes, deposited on the Au grating surface, reveal the presence of an additional plasmon-related absorption peak, located at longer wavelengths. The SPP absorption band is well evident even in the spectrum of the pristine Au grating and is slightly shifted after the deposition of gC_3N_4@MoS_2 (Fig. S7†). The plasmon triggering can efficiently contribute to charge carrier excitation as well as their effective separation and energy enrichment. In such a way, the catalytic activity of the flakes is enhanced, and longer light wavelengths can be also involved in the NRR. Thus, we can conclude that the Au/gC_3N_4@MoS_2 structure is able to utilize almost the full sunlight spectrum and potentially utilize the absorbed energy for the production of ammonia from nitrogen.

NRR with utilization of the Au/gC_3N_4@MoS_2 structure

First, in order to confirm the absence of plasmon-active substrate catalytic activity (*i.e.* nitrogen reduction on the gold grating surface without addition of gC_3N_4@MoS_2), control LSV measurements were performed (Fig. S6C†). In this case, the LSV curve inflections and shapes measured in the presence of both argon and nitrogen were almost the same, indicating that the plasmon active gold grating is catalytically inactive. So, all subsequently obtained results should be attributed to the redox activity of deposited gC_3N_4@MoS_2 flakes.

In the next step we proceed to the utilization of Au grating/gC_3N_4@MoS_2 samples for the NRR, performed in photo-electrochemical mode (Fig. 4) involving illumination with wide-spectrum simulated sunlight. First, the LSV curves were measured with electrolyte purging with argon and nitrogen (Fig. 4A). In the case of argon purged electrolyte, we observed the HER related on-set potential at −0.45 V. Utilization of sunlight illumination (also under argon purging) results in a slight shift of LSV curves, revealing the fact that the plasmon triggering activates gC_3N_4@MoS_2 redox activity. A significant change in LSV curve shape was observed when the electrolyte solution was saturated with nitrogen and the HER was partially blocked by the addition of ionic liquid. The onset potential was shifted from −0.29 V to −0.45 V *vs.* RHE, indicating the occurrence of some concurrent process to the HER process (with a high probability for the NRR). Even more pronounced shift of the LSV curve was observed with utilization of sunlight illumination and nitrogen purging. In this case the onset potential was shifted from −0.45 to −0.28 V *vs.* RHE, while the overpotential at 3 mA cm^{-2} was decreased by *ca.* 0.07 V. So, we can assume that the triggering with wide spectrum light increases the efficiency of the NRR. This phenomenon can be attributed to both, excitation of inner electrons in gC_3N_4@MoS_2 (with utilization of shorter wavelengths) and plasmon triggering (involving longer wavelengths).

A series of NRR tests were subsequently performed in the photo-electrochemical regime under different constant potentials (Fig. 4B). Experiments were followed by quantitative measurements of the amount of produced ammonia, performed by the photometric method (also taking into account the potential pH changes). As is evident, the Au/gC_3N_4@MoS_2 sample produces 640.3 μg h^{-1} mg_{cat}^{-1} μmol of ammonia (Fig. 4C) with utilization of −0.4 V external potential under simulated sunlight irradiation, which is 11.6 times higher than that measured in the dark (Fig. 4D). The NRR proceeds on the

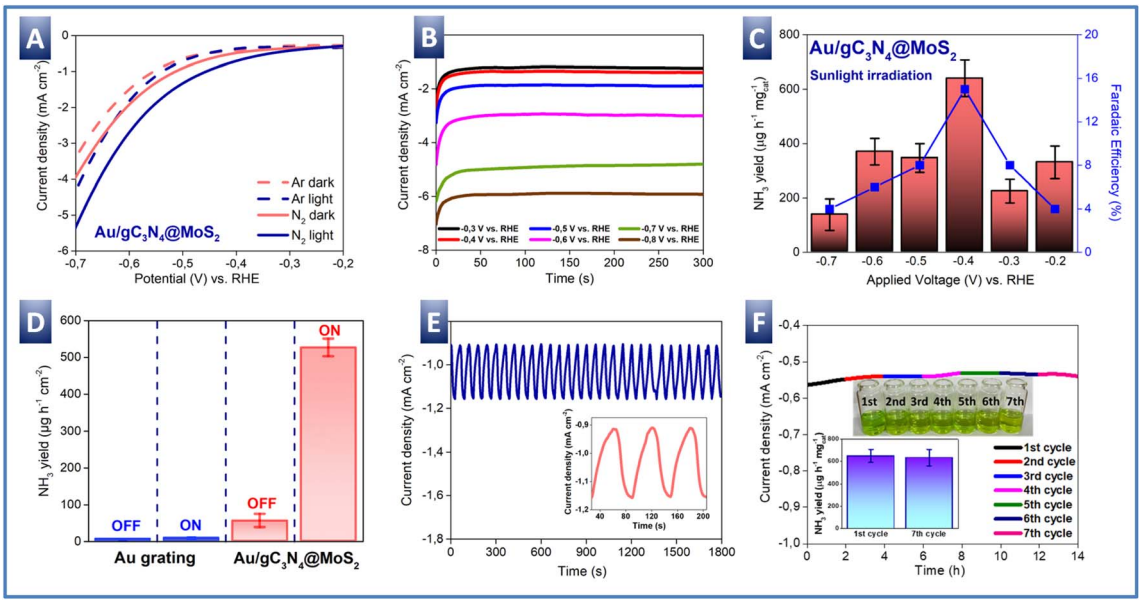

Fig. 4 (A) LSV curves of Au/gC_3N_4@MoS_2 utilized as the working electrode under N_2 and Ar bubbling in the dark or under illumination with simulated sunlight; (B) current densities measured in the chronoamperometry regime at different potentials; (C) NH_3 yield and faradaic efficiency, obtained on the Au/gC_3N_4@MoS_2 photoelectrode surface under different potentials; (D) yields of NH_3 obtained on the surface of the pristine Au grating and the Au/gC_3N_4@MoS_2 system with (ON) or without (OFF) sample illumination; (E) NRR performed in the light switch ON–OFF regime, and (F) long-term stability test of NRR activity of the Au/gC_3N_4@MoS_2 photoelectrode.

gC_3N_4@MoS_2 surface (the pristine Au grating shows almost no NRR activity – see Fig. 4D, in agreement with Fig. S6C†). So, it can be concluded that the light triggering (including both, direct or plasmon-assisted triggering of gC_3N_4@MoS_2 flakes) results in perfect NRR efficiency. Finally, calculated faradaic efficiency reaches the very good 15.1% value under the optimal experimental conditions (*i.e.* under sample illumination and application of −0.4 V external potential).

The impact of switching light on/off is additionally demonstrated in Fig. 4E, where an immediate increase of current density after switching light on and its decrease after the switching light off are demonstrated. Switching light on is also accompanied by an apparent decrease of charge transport resistance between the photoelectrode and nitrogen saturated electrolyte (Fig. S8†). The overall kinetics and speed of structure response to light illumination (in a "seconds" range) can suggest that plasmon assistance proceeds through the acceleration of the electronic process rather than through plasmon-assisted, material heating. Fig. 4F shows sample stability over 14 hours of continuous utilization in the photoelectrochemical regime. Only little changes in the current density as well as in the amount of ammonia produced (640.3 μg h^{-1} $mg_{cat}{}^{-1}$ before and 633.5 μg h^{-1} $mg_{cat}{}^{-1}$ after photo-electrode utilization) during the stability test period (Fig. S9B†) were observed. Additional measurements of the surface morphology and electrochemical activity (SEM-EDX and LSV) confirm the absence of the apparent changes of both parameters (Fig. S10†).

Control NRR experiments – impact of particular materials and plasmon assistance

We also performed a range of control experiments with the aim to estimate the particular contribution of used materials and highlight the role of plasmon triggering. First, utilization of Au/MoS_2 and Au/gC_3N_4 photoelectrodes instead of the Au/gC_3N_4@MoS_2 photoelectrode results in a significantly lower NRR efficiency due to the absence of redox-active centres (Au/gC_3N_4) or inefficient absorption of short light wavelengths (Fig. S11–S13†). A similar decrease in NRR efficiency, observed in the absence of a neighbouring Au grating (Fig. S12†), confirms the significant impact of plasmon triggering. A control hydrazine test during photoelectrochemical experiments with utilization of the Au/gC_3N_4@MoS_2 photo-electrode proves the absence of production of undesired compounds (Fig. S9†). In order to confirm the fact that ammonium cations are formed from nitrogen delivered to the solution from the air, NMR control experiments were performed with utilization of purging with $^{14}N_2$ or $^{15}N_2$ and $(^{14}NH_4)_2SO_4$ or $(^{15}NH_4)_2SO_4$ solutions as a control (Fig. S14†). From subsequently measured NMR spectra it is clear that created NH_3 really utilizes the delivered gas as a nitrogen source.[75–77]

NRR with utilization of the plasmon-coupled Au/gC_3N_4@MoS_2@MeNPs system – calculation results and structure optimization

In the next step, we proceed to plasmon triggering of gC_3N_4@MoS_2 NRR activity with utilization of coupled plasmon-active nanostructures. Unlike the previous case, such a system provides a higher enhancement of local plasmon strength in the space between the Au grating and plasmon-active nanoparticle(s), *i.e.*, in the place where gC_3N_4@MoS_2 flakes are located. For realization of the coupled plasmonic system, additional deposition of metal nanoparticles on the top of the Au/gC_3N_4@MoS_2 photo-electrode was used.

Before experiments, finite difference time domain (FDTD) and density functional (DFT) calculations were performed to estimate the impact of coupled plasmon triggering on the NRR efficiency and to optimize structure design.[71] The calculated distribution and local values of plasmon-related electric fields are presented in Fig. S15† as a function of different shapes and compositions of top-deposited nanoparticles (*i.e.* with a gC_3N_4@MoS_2 spacer between the Au grating and nanoparticles). The shapes of nanoparticles (spherical, triangle, cubic, and urchin-like) and their optical properties are summarized in Fig. S16.† As can be seen from the FDTD simulation, the local energy values in the presence of metal nanoparticles (coupled with the Au grating through the gC_3N_4@MoS_2 spacer) are several orders of magnitude higher than in the case of a simple grating. The best concentration of electric field energy in the gC_3N_4@MoS_2 location is found for cubic Au nanoparticles (Fig. S15†). This case is presented also in Fig. 5A, where a significant concentration of plasmon energy even inside gC_3N_4@MoS_2 flakes or in their nearby space is evident (unlike, for example, in the case of gold nanourchins). Thus, the most efficient plasmon triggering of gC_3N_4@MoS_2 catalytic activity could be expected with cubic gold nanoparticles. As is evident from the FDTD simulation, utilization of different nanoparticles results in a different value of the local electric field. In our DFT model, we used only the value of the electric field strength as a uniform field corresponding to a given type of nanoparticles or their absence.

Fig. 5B shows the particular NRR steps occurring on the gC_3N_4@MoS_2 surface (calculated using the DFT approach) with plasmon triggering (designated as a plasmon related electric field – $\vec{E}$, achieved on a simple grating or a grating coupled with Au nanocubes). According to a previous study,[72] the Mo edge sites of the MoS_2/gC_3N_4 heterostructure are energetically more favourable as the active sites for the reaction. During the relaxation of the geometry of the bilayer surface, the gC_3N_4 plane was curved in such a way that boundary effects arose near the binding site of the N_2 molecule on the edge of MoS_2, mainly manifested in the additional orientation of bound protons with subsequent correction of the binding energy. Although previous DFT studies of similar bilayer systems have considered the flat structure of gC_3N_4,[72] several other DFT studies of individual gC_3N_4 layers have produced curved surfaces consistent with that obtained in our calculations.[78–80] As shown in Fig. 5C (red line), in the free energy profile of sequential steps of the NRR in the absence of an external electric field, there are two main hydrogenation transitions corresponding to the potential determining steps (PDS) of the reaction. The first barrier with a height of 1.25 eV is associated with the formation of the *N–NH complex, and the second barrier with a height of 1.45 eV is related to the detachment of the first NH_3 molecule and the

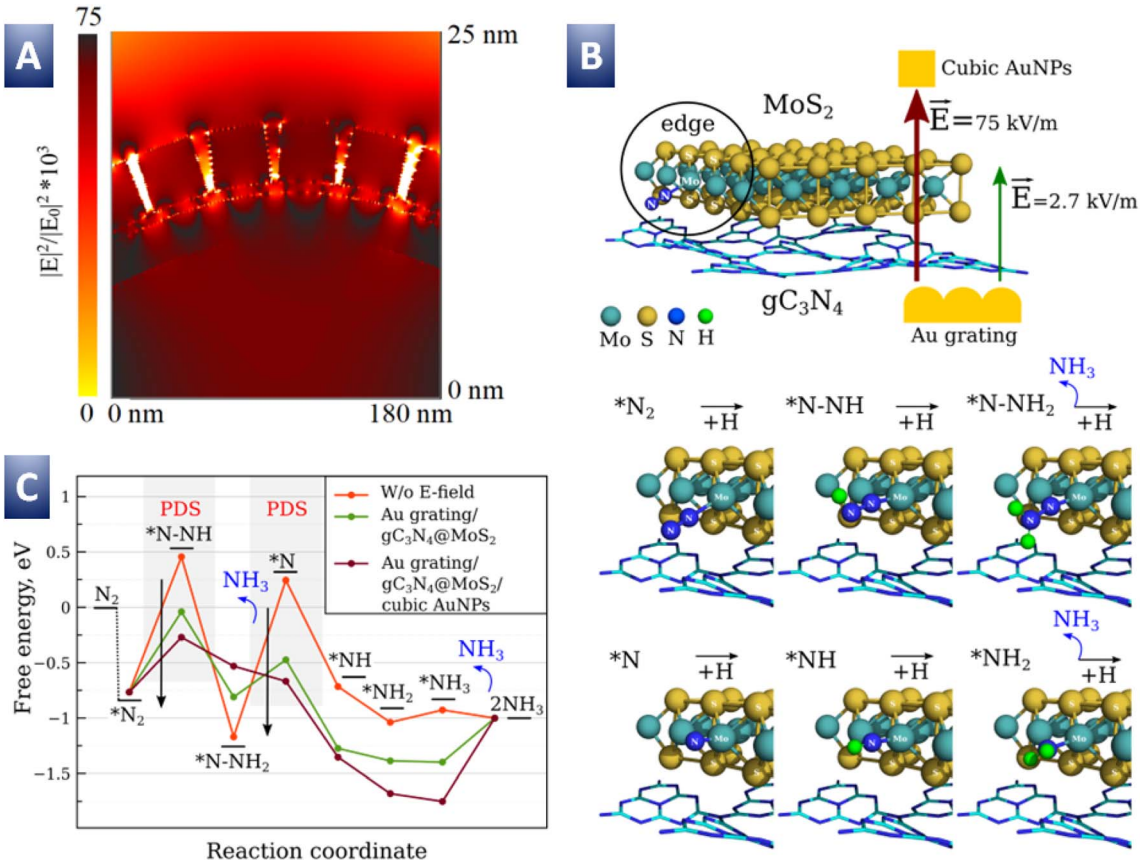

Fig. 5 (A) FDTD simulation of coupled plasmon energy distribution for the Au grating/gC_3N_4@MoS_2/cubic AuNPs structure case; (B) DFT simulation of the NRR process on the edge of the gC_3N_4@MoS_2 surface under external, plasmon-related $\vec{E}$; (C) free energy profile of the NRR with and without plasmon triggering in "simple" and coupled plasmon regimes.

formation of atomic nitrogen *N on the MoS_2 surface. However, even by triggering plasmons (a simple case of an Au grating is presented, which corresponds to a uniform e-field near the reaction site of 2.7 kV m^{-1}), the energy barrier at both stages can be reduced by 0.5 eV and 0.75 eV, respectively (Fig. 5B, green line).

In the case of the coupled plasmonic regime (*i.e.* combination of the Au grating and Au cubic nanoparticles) we obtained an electric field near the reaction site in the 12–75 kV m^{-1} range for various types of considered nanoparticles (Fig. S15† and 5A). Fig. 5C (brown line) shows the free energy profile of the NRR under conditions of an applied field of 75 kV m^{-1} (corresponding to utilization of cubic Au nanoparticles), at which an additional decrease in the first barrier by 0.25 eV and the second barrier by 0.2 eV is observed. The applied external, plasmon-related, electric field generally stabilizes the doublet states in the *N–NH, *N positions and destabilizes the singlet state in the *N–NH_2 position. This ratio in the influence of the electric field on the energy of singlet and doublet configurations of intermediates for a field of the order of 75 kV m^{-1} leads to an almost barrier-free NRR after the first PDS step, which may correspond to the significant increase in the chemical yield of NH_3 observed in the experiment.

NRR with utilization of the plasmon-coupled Au/gC_3N_4@MoS_2@MeNPs system – experimental results

Experimental verification of the calculation results was performed with utilization of different nanoparticles (Au or Ag) with various shapes in the first step (Fig. S16–S18†). In particular, the ammonia production yield was estimated as a function of top-deposited gold (spherical and multibranched shapes) and silver (spherical and triangular shapes) nanoparticles. Samples with silver nanoparticles show relatively low ammonia yields in the NRR process, in agreement with lower efficiency of plasmon coupling and additional negative impact of potential silver oxidation (and loss of plasmonic activity). In the case of spherical Au NPs, a relatively high efficiency was observed, due to the expected positive impact of coupled plasmon triggering. As can be expected, the best results were obtained in the case of cubic Au nanoparticles. Such type of nanoparticles can produce a large enhancement of the EF field, which is moreover shifted towards catalytic flakes. Utilization of Au nanourchins also led to a significant increase of the local electric field value, but without their "injection" in the gC_3N_4@MoS_2 location, which results in less efficient NRR (Fig. S15†).

The detailed characterization of the best sample structure (Au grating/gC_3N_4@MoS_2/cubic Au NPs, further designated as Au/gC_3N_4@MoS_2/AuNPs) is presented in Fig. 6. Fig. 6A and B

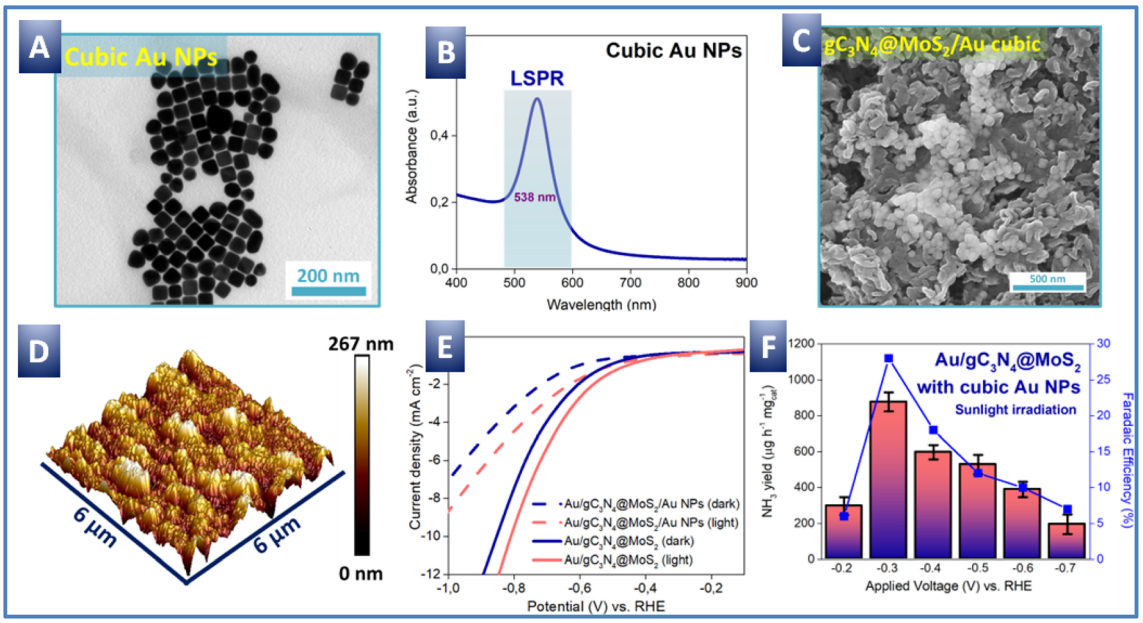

Fig. 6 (A) TEM image and (B) UV-Vis spectrum of cubic Au NPs; (C) SEM and (D) AFM images of Au/gC_3N_4@MoS_2 coupled with top-deposited cubic AuNPs; (E) LSV curves measured on the Au/gC_3N_4@MoS_2 and Au/gC_3N_4@MoS_2/AuNPs surface with and without light illumination; (F) NH_3 yield and faradaic efficiency obtained on the Au/gC_3N_4@MoS_2/AuNPs surface in the photoelectrochemical regime.

show the shape and optical properties of cubic AuNPs. TEM images show the homogeneous distribution and cubic shape of nanoparticles, with a size comparable with the "grating-like" surface pattern (*i.e.* nanoparticles are able to penetrate the grating valleys). The cubic AuNPs also efficiently absorb the light in the 500–600 wavelength range, due to plasmon excitation. This spectral location of the plasmon band can partially compensate the lower absorption windows of the Au/gC_3N_4@MoS_2 structure (Fig. 3A). The surface morphology of Au/gC_3N_4@MoS_2 after the deposition of cubic AuNPs is presented in Fig. 6C and D. The SEM image indicates the presence of 30–40 nm cubic gold nanoparticles on the sample surface (comparison of the gC_3N_4@MoS_2 surface before and after Au nanocube deposition is given in Fig. S19†). The changes of surface morphology are also evident from the AFM scan. Compared to the pristine Au grating or Au grating with deposited flakes, the deposition of cubic gold nanoparticles leads to slight flake re-orientation.

To verify the impact of coupled SPP–LSP triggering, the LSV curves were collected first (measurement of both Au/gC_3N_4@MoS_2/AuNPs and Au/gC_3N_4@MoS_2 samples is presented in Fig. 6E). It can be seen that in the dark the Au/gC_3N_4@MoS_2/AuNPs surface is slightly less catalytically active compared to Au/gC_3N_4@MoS_2, which effect can be explained by partial blocking of the gC_3N_4@MoS_2 surface by top-deposited nanoparticles. However, light triggering also has an apparent impact on the LSV curve shape in the case of plasmon coupling (*i.e.* in the Au/gC_3N_4@MoS_2/AuNPs case). Both onset and offset potentials were shifted towards lower (absolute) values. In turn, the amount of released ammonia and calculated faradaic efficiency are presented in Fig. 6F as a function of potential, used in photoelectrochemical experiments. As is evident, excellent NH_3

Table 2 Comparison of the present results with those previously published

Catalyst	Electrolyte	Potential (V *vs.* RHE)	NH_3 yield ($\mu g\ h^{-1}\ mg_{cat}^{-1}$)	FE (%)	Ref.
Zn^1N–C	0.1 M KOH	−0.3	16.1	11.8	81
Ru SAs/Ti_3C_2O	0.1 M HCl	−0.2	27.56	23.3	82
MXene/$TiFeO_x$	0.05 M H_2SO_4	−0.2	21.9	25.4	83
MoSAs–Mo_2C/NCNTs	5 mM H_2SO_4	−0.25	16.1	7.1	84
Ru/SnO_{2-x}	0.2 M K_2SO_4	−0.2	32.4	16.2	85
$FeMo_3S_4$	0.5 M $LiClO_4$	−0.3	65.3	19.2	86
$PdH_{0.43}$NRs	0.1 M Na_2SO_4	−0.2	17.53	18.6	87
CoPc–RGO 1D–2D	0.1 M K_2SO_4	−0.2	143.38	43.7	88
Fe_3C/Fe_3O_4@C-950	0.1 M HCl	−0.2	25.7	22.5	89
Au grating/gC_3N_4@MoS_2	0.1 M Na_2SO_4	−0.4	642.1	15.1	This work
Au grating/gC_3N_4@MoS_2/Au NPs	0.1 M Na_2SO_4	−0.3	882.1	28.1	This work

yield (882.1 μg h^{-1} mg_{cat}^{-1}) and faradaic efficiency (28.1%) were reached at the optimal potential, equal to −0.3 V (unlike the Au/gC_3N_4@MoS_2 case, where the optimal faradaic efficiency was reached at −0.4 V, which was 15.1%). So, utilization of plasmon coupling leads to a decrease in optimal potential, required for the NRR and simultaneously to an increase in faradaic efficiency, as well as in the overall ammonia production yield.

Finally, it should be noted that the results obtained in the coupled plasmonic regime overperform most of the previously published ones[81–89] in terms of both faradaic efficiency and ammonia yield (Table 2). Experimental results perfectly correlate with previous simulation of the Au grating – Au nanocube combination, where the plasmon related energy penetrates the gC_3N_4@MoS_2 space. The resulting high local electric field allows the redox activity of coupled gC_3N_4@MoS_2 to be significantly increased and decreased according to the energy demand of the NRR (despite some blocking of the gC_3N_4@MoS_2 surface by redox-inactive Au nanoparticles).

Conclusion

In this work, the rational design of a hero-photoelectrode for efficient NRR with light energy assistance is proposed. As a catalytic material, highly redox active, coupled gC_3N_4@MoS_2 2D flakes are used. Flakes were combined with plasmon-active nanostructures for efficient absorption and utilization of sunlight energy. Plasmon triggering was performed in two modes, with utilization of SPP-based triggering through the immobilization of the flakes on the surface of the plasmon-active Au grating or in the coupled plasmon regime, through the sandwiching of redox-active flakes between the Au grating and plasmon active nanoparticles (Au and Ag nanoparticles with different shapes were used). The FDTD simulation was used to estimate the local value of coupled plasmon strength and the local value of the plasmon-related electric field. The best penetration of coupled plasmon energy was predicted for the combination of the Au grating with cubic Au nanoparticles and the gC_3N_4@MoS_2 spacer between. In addition, the NRR process under plasmon triggering was simulated using a range of DFT calculations, also taking into account the FDTD results. Theoretical calculation indicates the ability to decrease the NRR energy demand (in particular – activation barrier of rate determining steps) under plasmon triggering, especially pronounced in the coupled plasmon regime. Theoretical results were subsequently verified in several experiments. In particular, with utilization of simple plasmon triggering (using solely the Au grating) we achieve 642.1 μg h^{-1} mg_{cat}^{-1} NH_3 production yield and 15.1% faradaic efficiency. The employment of plasmon coupling allows the decrease of the optimal NRR potential and simultaneous increase of the NH_3 production yield up to 882.1 μg h^{-1} mg_{cat}^{-1} and faradaic efficiency up to 28.1%.

Data availability

The data presented in this study are available **https://zenodo.org/records/12722224**.

Conflicts of interest

There are no conflicts to declare.

Acknowledgements

This work was supported by the GACR under project 23-08509S, by Project OP JAK_Amulet (no. CZ.02.01.01/00/22_008/0004558), supported by the Ministry of Education, Youth and Sports of the Czech Republic, co-funded by the European Union and by Academy of Finland under projects 340582 (R. R.) and 346369 (R. V.). This work was also partly supported by the Grant Agency of the Czech Technical University in Prague, grant no. SGS23/182/OHK3/3T/13.

References

1 J. Lim, C. A. Fernández, S. W. Lee and M. C. Hatzell, *ACS Energy Lett.*, 2021, **6**, 3676–3685.
2 M. J. Palys, H. Wang, Q. Zhang and P. Daoutidis, *Curr. Opin. Chem. Eng.*, 2021, **31**, 100667.
3 F. B. Juangsa, A. R. Irhamna and M. Aziz, *Int. J. Hydrogen Energy*, 2021, **46**, 14455–14477.
4 Z. Wan, Y. Tao, J. Shao, Y. Zhang and H. You, *Energy Convers. Manage.*, 2021, **228**, 113729.
5 A. T. Wijayanta, T. Oda, C. W. Purnomo, T. Kashiwagi and M. Aziz, *Int. J. Hydrogen Energy*, 2019, **44**, 15026–15044.
6 U. B. Shahid, Y. Bicer, S. Ahzi and A. Abdala, *Energy Convers. Manage.*, 2019, **198**, 111809.
7 A. R. Singh, B. A. Rohr, J. A. Schwalbe, M. Cargnello, K. Chan, T. F. Jaramillo, I. Chorkendorff and J. K. Nørskov, *ACS Catal.*, 2017, **7**, 706–709.
8 J. Humphreys, R. Lan and S. Tao, *Adv. Energy Sustainability Res.*, 2021, **2**, 2000043.
9 M. Wang, M. A. Khan, I. Mohsin, J. Wicks, A. H. Ip, K. Z. Sumon, C.-T. Dinh, E. H. Sargent, I. D. Gates and M. Golam Kibria, *Energy Environ. Sci.*, 2021, **14**, 2535–2548.
10 K. H. R. Rouwenhorst, A. G. J. Van der Ham and L. Lefferts, *Int. J. Hydrogen Energy*, 2021, **46**, 21566–21579.
11 G. Chehade and I. Dincer, *Fuel*, 2021, **299**, 120845.
12 H. Zhang, L. Wang, J. Van herle, F. Maréchal and U. Desideri, *Appl. Energy*, 2020, **259**, 114135.
13 G. Marnellos and M. Stoukides, *Science*, 1998, **282**, 98–100.
14 X. Guo, J. Gu, S. Lin, S. Zhang, Z. Chen and S. Huang, *J. Am. Chem. Soc.*, 2020, **142**, 5709–5721.
15 Y. Li, H. Wang, C. Priest, S. Li, P. Xu and G. Wu, *Adv. Mater.*, 2021, **33**, 2000381.
16 L. Zhang, X. Ji, X. Ren, Y. Ma, X. Shi, Z. Tian, A. M. Asiri, L. Chen, B. Tang and X. Sun, *Adv. Mater.*, 2018, **30**, 1800191.
17 J. Sun, W. Kong, Z. Jin, Y. Han, L. Ma, X. Ding, Y. Niu and Y. Xu, *Chin. Chem. Lett.*, 2020, **31**, 953–960.
18 C. Yang, Y. Zhu, J. Liu, Y. Qin, H. Wang, H. Liu, Y. Chen, Z. Zhang and W. Hu, *Nano Energy*, 2020, **77**, 105126.
19 S. Niu, *J. Energy Chem.*, 2023, **86**, 69–83.
20 W. Zang, T. Yang, H. Zou, S. Xi, H. Zhang, X. Liu, Z. Kou, Y. Du, Y. P. Feng, L. Shen, L. Duan, J. Wang and S. J. Pennycook, *ACS Catal.*, 2019, **9**, 10166–10173.

21 Y.-X. Lin, S.-N. Zhang, Z.-H. Xue, J.-J. Zhang, H. Su, T.-J. Zhao, G.-Y. Zhai, X.-H. Li, M. Antonietti and J.-S. Chen, *Nat. Commun.*, 2019, **10**, 4380.
22 W. Peng, M. Luo, X. Xu, K. Jiang, M. Peng, D. Chen, T.-S. Chan and Y. Tan, *Adv. Energy Mater.*, 2020, **10**, 2001364.
23 X. Wang, S. Qiu, J. Feng, Y. Tong, F. Zhou, Q. Li, L. Song, S. Chen, K.-H. Wu, P. Su, S. Ye, F. Hou, S. X. Dou, H. K. Liu, G. Q. (Max) Lu, C. Sun, J. Liu and J. Liang, *Adv. Mater.*, 2020, **32**, 2004382.
24 S. Mukherjee, X. Yang, W. Shan, W. Samarakoon, S. Karakalos, D. A. Cullen, K. More, M. Wang, Z. Feng, G. Wang and G. Wu, *Small Methods*, 2020, **4**, 1900821.
25 K. Chu, Y. Liu, Y. Li, J. Wang and H. Zhang, *ACS Appl. Mater. Interfaces*, 2019, **11**, 31806–31815.
26 H. Jin, L. Li, X. Liu, C. Tang, W. Xu, S. Chen, L. Song, Y. Zheng and S.-Z. Qiao, *Adv. Mater.*, 2019, **31**, 1902709.
27 J. Liu, X. Kong, L. Zheng, X. Guo, X. Liu and J. Shui, *ACS Nano*, 2020, **14**, 1093–1101.
28 H. Li, J. Shang, Z. Ai and L. Zhang, *J. Am. Chem. Soc.*, 2015, **137**, 6393–6399.
29 D. Yan, H. Li, C. Chen, Y. Zou and S. Wang, *Small Methods*, 2019, **3**, 1800331.
30 Y. Yang, R. Wang, L. Yang, Y. Jiao and T. Ling, *Chem. Commun.*, 2020, **56**, 14154–14162.
31 H. Yu Zhou, J. Chen Li, Z. Wen and Q. Jiang, *Phys. Chem. Chem. Phys.*, 2019, **21**, 14583–14588.
32 Y. Xiao, X. Tan, Y. Guo, J. Chen, W. He, H. Cui and C. Wang, *J. Energy Chem.*, 2023, **87**, 400–407.
33 Y. Sun, Y. Han, X. Zhang, W. Cai, Y. Zhang, Y. Zhang, Z. Li, B. Li, J. Lai and L. Wang, *Appl. Catal., B*, 2022, **319**, 121933.
34 L. Li, C. Tang, X. Cui, Y. Zheng, X. Wang, H. Xu, S. Zhang, T. Shao, K. Davey and S.-Z. Qiao, *Angew. Chem., Int. Ed.*, 2021, **133**, 14250–14256.
35 A. U. Shetty and R. Sankannavar, *J. Energy Chem.*, 2024, **92**, 681–697.
36 J. Choi, B. H. R. Suryanto, D. Wang, H.-L. Du, R. Y. Hodgetts, F. M. Ferrero Vallana, D. R. MacFarlane and A. N. Simonov, *Nat. Commun.*, 2020, **11**, 5546.
37 X. Zhao, G. Hu, G.-F. Chen, H. Zhang, S. Zhang and H. Wang, *Adv. Mater.*, 2021, **33**, 2007650.
38 Y. Sun, Y. Ahmadi, K.-H. Kim and J. Lee, *Renewable Sustainable Energy Rev.*, 2022, **170**, 112967.
39 L. Zhang, S. Hou, T. Wang, S. Liu, X. Gao, C. Wang and G. Wang, *Small*, 2022, **18**, 2202252.
40 X. Li, H. Shi, S. Zuo, B. Gao, C. Han, T. Wang, C. Yao and C. Ni, *Chem. Eng. J.*, 2021, **414**, 128797.
41 B. Sun, P. Qiu, Z. Liang, Y. Xue, X. Zhang, L. Yang, H. Cui and J. Tian, *Chem. Eng. J.*, 2021, **406**, 127177.
42 J. Kim, C. H. Lee, Y. H. Moon, M. H. Lee, E. H. Kim, S. H. Choi, Y. J. Jang and J. S. Lee, *J. Energy Chem.*, 2023, **84**, 394–401.
43 Y. J. Jang, A. E. Lindberg, M. A. Lumley and K.-S. Choi, *ACS Energy Lett.*, 2020, **5**, 1834–1839.
44 X. Fu, J. B. Pedersen, Y. Zhou, M. Saccoccio, S. Li, R. Sažinas, K. Li, S. Z. Andersen, A. Xu, N. H. Deissler, J. B. V. Mygind, C. Wei, J. Kibsgaard, P. C. K. Vesborg, J. K. Nørskov and I. Chorkendorff, *Science*, 2023, **379**, 707–712.
45 M. A. Mushtaq, M. Arif, G. Yasin, M. Tabish, A. Kumar, S. Ibraheem, W. Ye, S. Ajmal, J. Zhao, P. Li, J. Liu, A. Saad, X. Fang, X. Cai, S. Ji and D. Yan, *Renewable Sustainable Energy Rev.*, 2023, **176**, 113197.
46 D. Zabelin, A. Zabelina, E. Miliutina, A. Trelin, R. Elashnikov, D. Nazarov, M. Maximov, Y. Kalachyova, P. Sajdl, J. Lancok, M. Vondracek, V. Svorcik and O. Lyutakov, *Chem. Eng. J.*, 2022, **443**, 136440.
47 S. Fang, M. Rahaman, J. Bharti, E. Reisner, M. Robert, G. A. Ozin and Y. H. Hu, *Nat. Rev. Methods Primers*, 2023, **3**, 1–21.
48 H. Zhao, L. Jian, M. Gong, M. Jing, H. Li, Q. Mao, T. Lu, Y. Guo, R. Ji, W. Chi, Y. Dong and Y. Zhu, *Small Struct.*, 2022, **3**, 2100229.
49 A. Sudhaik, A. A. Parwaz Khan, P. Raizada, V.-H. Nguyen, Q. Van Le, A. M. Asiri and P. Singh, *Chemosphere*, 2022, **291**, 132781.
50 Q. Li, Z. Zhao, X. Bai, X. Tong, S. Yue, J. Luo, X. Yu, Z. Wang, Z. Wang, P. Li, Y. Liang and Z. Wang, *Chin. J. Catal.*, 2021, **42**, 1763–1771.
51 G. Bharath, C. Liu, F. Banat, A. Kumar, A. Hai, A. Kumar Nadda, V. Kumar Gupta, M. Abu Haija and J. Balamurugan, *Chem. Eng. J.*, 2023, **465**, 143040.
52 Y. Peng, J. Albero, A. Franconetti, P. Concepción and H. García, *ACS Catal.*, 2022, **12**, 4938–4946.
53 P. Subramanyam, B. Meena, V. Biju, H. Misawa and S. Challapalli, *J. Photochem. Photobiol., C*, 2022, **51**, 100472.
54 D. Zabelin, K. Severa, J. Kuličeк, B. Rezek, A. Tulupova, R. Elashnikov, A. Zabelina, V. Burtsev, P. Sajdl, E. Miliutina, V. Svorcik and O. Lyutakov, *ACS Appl. Mater. Interfaces*, 2023, **15**, 29072–29083.
55 A. Abdullah, M. A. Johar, A. Waseem, I. V. Bagal, M. A. Hassan, J. K. Lee and S.-W. Ryu, *Mater. Sci. Eng., B*, 2022, **275**, 115514.
56 X. Sun, Z. Chen, Y. Shen, J. Lu, Y. Shi, Y. Cui, F. Guo and W. Shi, *J. Colloid Interface Sci.*, 2023, **652**, 1016–1027.
57 M. Ali, F. Zhou, K. Chen, C. Kotzur, C. Xiao, L. Bourgeois, X. Zhang and D. R. MacFarlane, *Nat. Commun.*, 2016, **7**, 11335.
58 C. Hu, X. Chen, J. Jin, Y. Han, S. Chen, H. Ju, J. Cai, Y. Qiu, C. Gao, C. Wang, Z. Qi, R. Long, L. Song, Z. Liu and Y. Xiong, *J. Am. Chem. Soc.*, 2019, **141**, 7807–7814.
59 M. Nazemi and M. A. El-Sayed, *Nano Energy*, 2019, **63**, 103886.
60 L.-W. Chen, Y.-C. Hao, Y. Guo, Q. Zhang, J. Li, W.-Y. Gao, L. Ren, X. Su, L. Hu, N. Zhang, S. Li, X. Feng, L. Gu, Y.-W. Zhang, A.-X. Yin and B. Wang, *J. Am. Chem. Soc.*, 2021, **143**, 5727–5736.
61 H. Bai, S. H. Lam, J. Yang, X. Cheng, S. Li, R. Jiang, L. Shao and J. Wang, *Adv. Mater.*, 2022, **34**, 2104226.
62 T.-A. Bu, Y.-C. Hao, W.-Y. Gao, X. Su, L.-W. Chen, N. Zhang and A.-X. Yin, *Nanoscale*, 2019, **11**, 10072–10079.
63 L. Ma, Y.-L. Chen, X.-P. Song, D.-J. Yang, H.-X. Li, S.-J. Ding, L. Xiong, P.-L. Qin and X.-B. Chen, *ACS Appl. Mater. Interfaces*, 2020, **12**, 38554–38562.
64 J. Xu, Y. Si, Z. Li, S. Jiang, X. Xiu, F. Lei, X. Du, B. Man, J. Yu and C. Zhang, *Appl. Surf. Sci.*, 2021, **544**, 148908.

65 L. Ma, Y.-L. Chen, D.-J. Yang, S.-J. Ding, L. Xiong, P.-L. Qin and X.-B. Chen, *J. Phys. Chem. C*, 2020, **124**, 25473–25479.
66 P. Dey, T. A. Tabish, S. Mosca, F. Palombo, P. Matousek and N. Stone, *Small*, 2020, **16**, 1906780.
67 Z. Cao, P. He, T. Huang, S. Yang, S. Han, X. Wang and G. Ding, *Chem. Mater.*, 2020, **32**, 3813–3822.
68 X. Liu, A. Dang, T. Li, Y. Sun, T.-C. Lee, W. Deng, S. Wu, A. Zada, T. Zhao and H. Li, *ACS Sens.*, 2023, **8**, 1287–1298.
69 R. Tan, A. Sivanantham, B. Jansi Rani, Y. J. Jeong and I. S. Cho, *Coord. Chem. Rev.*, 2023, **494**, 215362.
70 G. H. Han, J. Bang, G. Park, S. Choe, Y. J. Jang, H. W. Jang, S. Y. Kim and S. H. Ahn, *Small*, 2023, **19**, 2205765.
71 A. Zabelina, E. Miliutina, J. Dedek, A. Trelin, D. Zabelin, R. Valiev, R. Ramazanov, V. Burtsev, D. Popelkova, M. Stastny, V. Svorcik and O. Lyutakov, *ACS Catal.*, 2023, **13**, 10916–10926.
72 K. Chu, Y. Liu, Y. Li, Y. Guo and Y. Tian, *ACS Appl. Mater. Interfaces*, 2020, **12**, 7081–7090.
73 K. Chu, J. Wang, Y. Liu and Z. Geng, *Carbon*, 2018, **140**, 112–123.
74 J. Hu, C. Zhang, L. Jiang, H. Lin, Y. An, D. Zhou, M. K. H. Leung and S. Yang, *Joule*, 2017, **1**, 383–393.
75 S. Z. Andersen, V. Čolić, S. Yang, J. A. Schwalbe, A. C. Nielander, J. M. McEnaney, K. Enemark-Rasmussen, J. G. Baker, A. R. Singh, B. A. Rohr, M. J. Statt, S. J. Blair, S. Mezzavilla, J. Kibsgaard, P. C. K. Vesborg, M. Cargnello, S. F. Bent, T. F. Jaramillo, I. E. L. Stephens, J. K. Nørskov and I. Chorkendorff, *Nature*, 2019, **570**, 504–508.
76 R. Y. Hodgetts, A. S. Kiryutin, P. Nichols, H.-L. Du, J. M. Bakker, D. R. Macfarlane and A. N. Simonov, *ACS Energy Lett.*, 2020, **5**, 736–741.
77 M. Sun, C. Ma, M. Ma, Y. Wei, S. Dong, X. Zhang, J. Tian and M. Shao, *Mater. Today Phys.*, 2023, **30**, 100945.
78 L. Miguel Azofra, D. R. MacFarlane and C. Sun, *Phys. Chem. Chem. Phys.*, 2016, **18**, 18507–18514.
79 L. Kang, M. Zhu and Y. Zhao, *Catalysts*, 2019, **9**, 887.
80 X. Zhou, M. Zhu and L. Kang, *Catalysts*, 2019, **9**, 808.
81 Y. Kong, Y. Li, X. Sang, B. Yang, Z. Li, S. Zheng, Q. Zhang, S. Yao, X. Yang, L. Lei, S. Zhou, G. Wu and Y. Hou, *Adv. Mater.*, 2022, **34**, 2103548.
82 G. Chen, M. Ding, K. Zhang, Z. Shen, Y. Wang, J. Ma, A. Wang, Y. Li and H. Xu, *ChemSusChem*, 2022, **15**, e202102352.
83 Y. Guo, T. Wang, Q. Yang, X. Li, H. Li, Y. Wang, T. Jiao, Z. Huang, B. Dong, W. Zhang, J. Fan and C. Zhi, *ACS Nano*, 2020, **14**, 9089–9097.
84 Y. Ma, T. Yang, H. Zou, W. Zang, Z. Kou, L. Mao, Y. Feng, L. Shen, S. J. Pennycook, L. Duan, X. Li and J. Wang, *Adv. Mater.*, 2020, **32**, 2002177.
85 J. Zheng, K. Yu, S. Yuan, L. Xiang, K. Wang, S. Jing and N. Li, *J. Alloys Compd.*, 2023, **962**, 171028.
86 J. Wang, H. Nan, Y. Tian and K. Chu, *ACS Sustainable Chem. Eng.*, 2020, **8**, 12733–12740.
87 Z. Wang, Z. Dai, S. Wang, H. Zhang, W. Tian, Y. Xu, X. Li, L. Wang and H. Wang, *Chem. Eng. J.*, 2021, **416**, 129105.
88 S. Paul, S. Sarkar, A. Adalder, S. Kapse, R. Thapa and U. K. Ghorai, *ACS Sustainable Chem. Eng.*, 2023, **11**, 6191–6200.
89 X. Yang, Y. Tian, S. Mukherjee, K. Li, X. Chen, J. Lv, S. Liang, L.-K. Yan, G. Wu and H.-Y. Zang, *Angew. Chem., Int. Ed.*, 2023, **62**, e202304797.